Philosophical Magazine,
Vol. 87, No. 34, 1 December 2007, 5447–5459

Taylor & Francis
Taylor & Francis Group

TEM and STEM investigation of grain boundaries and second phases in barium titanate

S. J. ZHENG†‡, K. DU*†, X. H. SANG†‡ and X. L. MA†

†Shenyang National Laboratory for Materials Science, Institute of Metal Research, Chinese Academy of Sciences, 72 Wenhua Road, 110016 Shenyang, China
‡Graduate School of Chinese Academy of Sciences, 100049 Beijing, China

(*Received 5 June 2007; in final form 26 August 2007*)

An intergranular layer was found in 0.4 mol% Y-doped $BaTiO_3$, which was sintered below the eutectic temperature in air. The layer possessed a crystal structure similar to $Ba_6Ti_{17}O_{40}$ with a thickness of 0.7 nm. Plate-like second phases of $Ba_6Ti_{17}O_{40}$ were also observed at triple-grain junctions and an orientation relationship of $(1\bar{1}\bar{1})_t//(001)_m$, $(1\bar{1}2)_t//(60\bar{2})_m$ and $[110]_t//[0\bar{1}0]_m$ was determined between the tetragonal $BaTiO_3$ and the monoclinic $Ba_6Ti_{17}O_{40}$. The detailed structure of the interface between $BaTiO_3$ and $Ba_6Ti_{17}O_{40}$ was resolved by scanning transmission electron microscopy and high-resolution transmission electron microscopy investigations.

1. Introduction

$BaTiO_3$-based compounds are one of the most important electronic ceramics, which have numerous applications in sensors, multilayer ceramic capacitors and tuneable microwave devices [1–3]. For example, Y-doped $BaTiO_3$ ceramics, with their excellent positive temperature coefficient of resistivity (PTC), are widely used as commercial thermistors. It is generally accepted that the electrical properties of the $BaTiO_3$ ceramics, particularly the PTC effect, are closely related to their grain boundaries (GBs) [4–7]. Intensive studies have been performed on the GB structures in $BaTiO_3$ ceramics in the development of materials and to understand the electrical behaviour of barium titanate compounds [8–16].

Although grain boundary films commonly occur in ceramics, most studies on barium titanates by transmission electron microscopy (TEM) failed to demonstrate the presence of grain boundary films [11, 15, 17]. However, Lee *et al.* [8] found an intermediate phase with a nominal composition of $BaTi_2O_5$ at the GBs of $BaTiO_3$ in abnormal grain growth with TiO_2-excess $BaTiO_3$ using high-resolution transmission electron microscopy (HRTEM) and electron-energy loss spectroscopy (EELS). Nonetheless, the structure of the intermediate phase was not resolved from HRTEM images. As no amorphous phase was found in their sample and the sintering temperature (1250°C) was well below the eutectic temperature of the second phase $Ba_6Ti_{17}O_{40}$ (1332 C), it was proposed that the $BaTiO_3$ grains had abnormally grown

*Corresponding author. Email: kuidu@imr.ac.cn

Philosophical Magazine
ISSN 1478–6435 print/ISSN 1478–6443 online © 2007 Taylor & Francis
http://www.tandf.co.uk/journals
DOI: 10.1080/14786430701654386

into a polyhedral shape with the assistance of the intermediate phase but not a liquid phase as generally believed [8]. Similarly, Yamamoto and co-workers [9, 10] observed an ordered structure at faceted GBs of TiO_2-excess $BaTiO_3$, which was assumed to be a rutile-like structure by electron loss near-edge structure (ELNES) analysis.

In TiO_2-excess $BaTiO_3$-based compounds, second phase $Ba_6Ti_{17}O_{40}$ was often observed at GBs or crystal defects inside matrix grains [18–21]. The orientation relationship between the tetragonal $BaTiO_3$ and the monoclinic $Ba_6Ti_{17}O_{40}$ was mostly measured as $(\bar{1}1\bar{1})_t//(001)_m$, $(001)_t//(\bar{1}0\bar{1})_m$ $(1\bar{1}0)_t//(20\bar{6})_m$, $[001]_t//[0\bar{1}0]_m$ [18, 20–22]. Nevertheless, all 12 possible orientation relationships, which satisfy $(111)_t//(001)_m$ and $[1\bar{1}0]_t//[010]_m$, were also reported by X-ray diffraction pole figure analysis on polycrystalline $Ba_6Ti_{17}O_{40}$ reactively formed on a single crystal $BaTiO_3$ substrate [23].

In this work, we have studied the GBs and second phase in a Y-doped $BaTiO_3$ by TEM and scanning transmission electron microscopy (STEM). An intergranular layer was found at faceted GBs in the material and high-resolution Z-contrast imaging was employed to resolve the detailed structure of the layer as well as the interface between the second phase and the $BaTiO_3$ grain.

2. Experimental

Y-doped $BaTiO_3$ was prepared by the conventional mixed-oxide method. The appropriate amounts of $BaCO_3$, TiO_2 and Y_2O_3 powders (with purities of 99.99, 99.99 and 99%, respectively, provided by Sinopharm Chemical Reagent Ltd., Beijing, China) were mixed at the atomic ratio of $Ba/Ti/Y = 1.000:1.001:0.004$. The mixture was calcined at 1050°C for 30 h and milled in an agate mortar. Thereafter, the powders were dry-pressed into pellets (diameter 20 mm and thickness 1 mm) at a pressure of 20 MPa. The pellets were then sintered in air at 1250 and 1300°C over 24 and 10 h. The nominal heating and cooling rates were 5°C/min for the whole experiment.

The microstructure of the doped $BaTiO_3$ was studied using a Tecnai F30 (scanning) transmission electron microscope (FEI Co., Hillsboro, OR, USA), a JEM 2010 transmission electron microscope (JEOL, Tokyo, Japan) and a MEF4A optical microscope (Leica, Wein, Austria). Electron microscopy specimens were prepared by cutting, grinding and ion-milling, while optical microscopy specimens were polished and etched in a $H_2O/HCl/HF$ (95:4:1, v/v) solution. The Tecnai F30 electron microscope was equipped with an X-ray energy dispersive spectrometer (EDS) and a Gatan imaging filter (GIF) system for chemical analysis plus a high-angle annular dark-field (HAADF) detector for *Z*-contrast imaging. The size of the electron probe for chemical analysis was about 1 nm.

High-resolution *Z*-contrast imaging is performed by scanning an electron probe across the crystalline specimens oriented in the zone axis while collecting the transmitted electrons with the HAADF detector (at an angle range of 60–227 mrad) at the same rate. The intensity of the images is approximately proportional to the mean square atomic number (Z) in the volumes examined by the electron probe. Accordingly, images of this type are known as *Z*-contrast images [24, 25]. As the

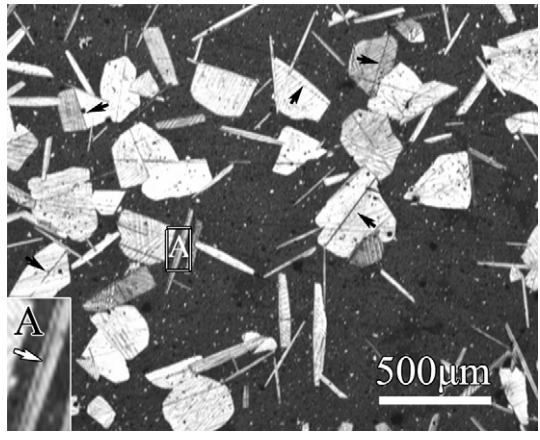

Figure 1. Optical micrograph showing the microstructure of Y-doped $BaTiO_3$. The inset is an enlargement of the region marked with A, which presents a twin lamella located in the middle of a plate-like abnormal grain. Twin lamellae in equiaxed abnormal grains are indicated by arrows.

collected signals can be treated as incoherent using high-angle annular dark-field detection, the image can be considered as a convolution of the specimen object function with the intensity distribution in the incident probe [24–27]. Hence, by the use of the maximum entropy method [28, 29], object functions were retrieved from *Z*-contrast images to obtain the positional and intensity information of the atoms in the specimens at a high accuracy.

3. Results

Figure 1 shows a typical microstructure of the Y-doped $BaTiO_3$. It is clear that abnormal grain growth occurred in the sample. The abnormal grains had either a plate-like or an equiaxed shape, which was confirmed by optical microscopy on a series of interior sections. Here, the sections were obtained by grinding and polishing materials from the sintering surface through a series of depths in the sample at an increment of 100 μm. Twin lamellae (indicated by arrows in figure 1) can be seen in nearly all the abnormal grains, where the abnormal plate-like grains were elongated along the twin planes and the equiaxed shape grains often contained one or more twin lamellae, which could be parallel or nonparallel to each other. From the optical and electron micrographs, the average size of the abnormal grains was estimated at ~200 μm compared to matrix grains of ~0.3 μm. The TEM study revealed that the abnormal GBs (the boundaries between abnormal, coarse grains and normal, fine grains; figure 2a) were faceted with long segments parallel to the {111} planes and small steps parallel to the {110} planes of $BaTiO_3$. Many matrix GBs (the boundaries between normal fine grains; figure 2b) also form facets; for example, figure 3 shows an edge-on matrix GB, which decomposed into two types of facets whose habit

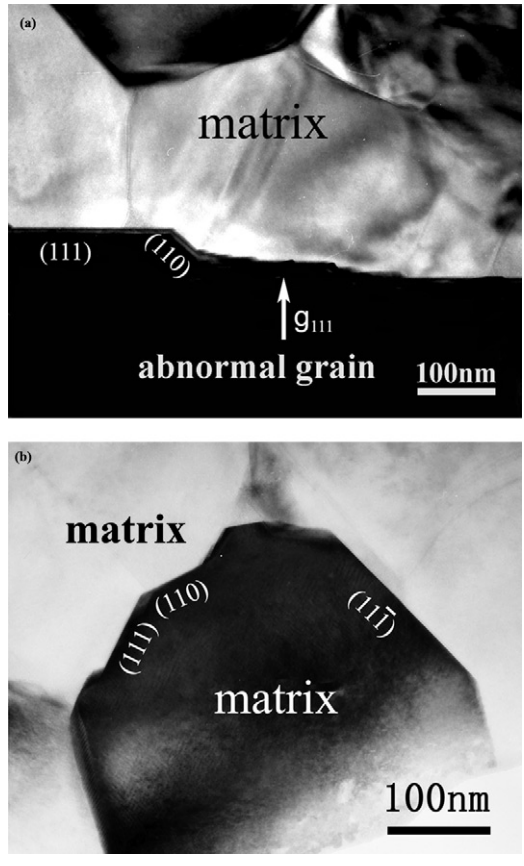

Figure 2. Bright-field transmission electron micrographs (TEM) of a faceted abnormal GB (a) and matrix GB (b).

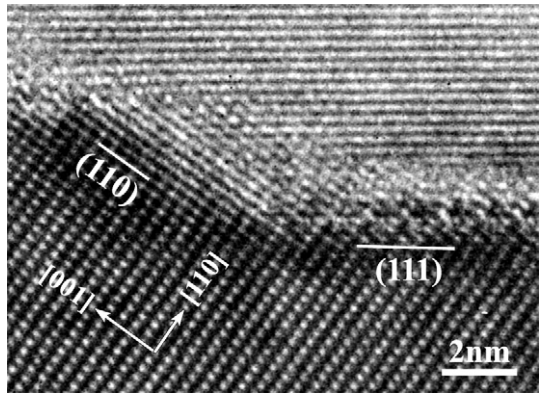

Figure 3. High-resolution transmission electron micrograph (HRTEM) of a faceted matrix GB.

planes were $\{111\}_t$ and $\{110\}_t$ of the $BaTiO_3$ grain at one side of the GB but high index planes at the other side.

The $Ba_6Ti_{17}O_{40}$ second phase was located at a triple junction of the $BaTiO_3$ grains. Figure 4a shows a $Ba_6Ti_{17}O_{40}$ second phase sited between two matrix grains A and B, and an abnormal grain C. The second phase has a plate-like shape and forms a planar boundary with the abnormal grain in the longitudinal direction. Note that the planar boundary runs straight across the triple-grain junction and the second phase itself protrudes from the planar boundary into the matrix grains A and B. A select-area diffraction pattern (SADP; figure 4b) was taken from the triple-grain junction with the monoclinic $Ba_6Ti_{17}O_{40}$ second phase tilted to the $[0\bar{1}0]_m$ zone axis. The weaker reflections came from the second phase and the stronger reflections from the abnormal $BaTiO_3$ grain at the $[110]_t$ zone axis. The coincident reflections in the SADP indicated parallel planes between the tetragonal $BaTiO_3$ and the monoclinic $Ba_6Ti_{17}O_{40}$. These parallel planes are $(1\bar{1}\bar{1})_t//(001)_m$, $(1\bar{1}2)_t//(60\bar{2})_m$, while the parallel axis is $[110]_t//[0\bar{1}0]_m$. The triple-grain junction was also tilted to the $[3\bar{5}0]_m$ zone axis of $Ba_6Ti_{17}O_{40}$. The corresponding SADP (figure 4c) suggested that the $[321]_t$ zone axis of $BaTiO_3$ is parallel to the $[3\bar{5}0]_m$ of $Ba_6Ti_{17}O_{40}$. Hence, an orientation relationship was determined for $(1\bar{1}\bar{1})_t//(001)_m$, $(1\bar{1}2)_t//(60\bar{2})_m$, and $[110]_t//[0\bar{1}0]_m$ between $BaTiO_3$ and $Ba_6Ti_{17}O_{40}$, where the parallel axis of $[321]_t//[3\bar{5}0]_m$ is consistent with this orientation relationship. The concentration of Y and Si in the second phase was below the detection limit of the EDS analysis.

Z-contrast imaging was performed on the planar boundary between the $BaTiO_3$ abnormal grain and $Ba_6Ti_{17}O_{40}$ second phase (figure 5). As the atomic number of Ba (56) is much higher than either Ti (22) or O (8), the bright spots in the image are directly related to the Ba atom columns in the material. It clearly shows that, instead of being straight along the $\{111\}_t$ plane of $BaTiO_3$, the boundary actually facets onto the $\{110\}_t$ and $\{001\}_t$ planes. These steps indicate that it is energetically more favourable for the $\{110\}_t$ and $\{001\}_t$ planes than the $\{111\}_t$ plane of $BaTiO_3$ at the boundary between $BaTiO_3$ and $Ba_6Ti_{17}O_{40}$. Using the coordinates of Ba atoms, determined from the *Z*-contrast image, and placing the Ti and O atoms by following the structure models of $BaTiO_3$ and $Ba_6Ti_{17}O_{40}$, a structure model was deduced (figure 5d) for the boundary of the $BaTiO_3$ grain and $Ba_6Ti_{17}O_{40}$ second phase. A distortion of the unit cell of $Ba_6Ti_{17}O_{40}$ in the *Z*-contrast image is due to a constant specimen drift during the long acquisition time, although the actual shape of the unit cell can be seen in the corresponding HRTEM image (figure 6).

The monoclinic unit cell of $Ba_6Ti_{17}O_{40}$ can be considered as a construction of eight $(001)_m$ layers stacked along the $[001]_m$ direction as described in [22, 30]. Here, we will use the same number as in [22] to denote the $(001)_m$ layers in $Ba_6Ti_{17}O_{40}$. In successive $(001)_m$ layers, the number of Ba atoms in the unit length along the $[0\bar{1}0]_m$ direction is different [22]. Therefore, the image intensity varies in different $(001)_m$ layers as shown in the *Z*-contrast image of the $Ba_6Ti_{17}O_{40}$ along the $[0\bar{1}0]_m$ direction. However, at the boundary region, the presence of strain near the boundary, as well as other effects, such as disordered scattering and dechannelling effects, could increase or decrease the intensity of the *Z*-contrast image; thus, the image intensity could not be simply related to the occupation of Ba atoms [24, 31]. Nevertheless, qualitative interpretation of the image intensity remains applicable on a local scale. Compared to the region of bulk $Ba_6Ti_{17}O_{40}$ (top region of figure 5), it can be seen

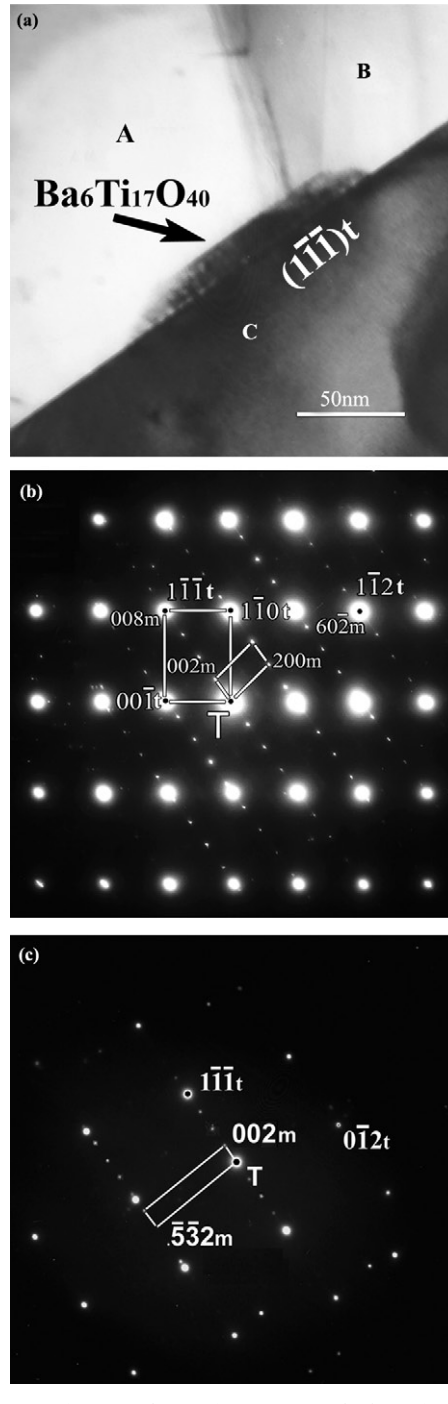

Figure 4. Bright-field TEM image of $Ba_6Ti_{17}O_{40}$ second phase located at the triple junction of $BaTiO_3$ grains (a). Corresponding select-area diffraction patterns (SADP) of the triple grain-junction, where $BaTiO_3$ grain C was orientated to the $[110]_t$ (b) and the $[321]_t$ (c) directions.

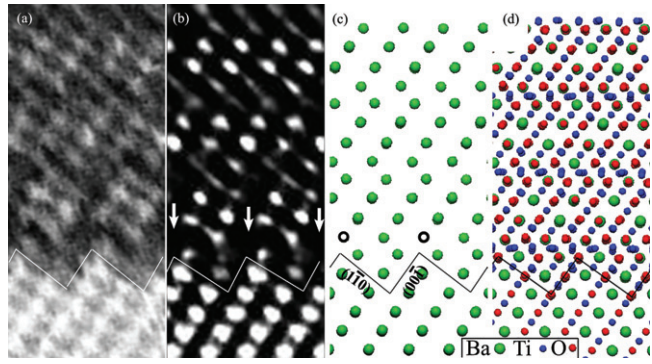

Figure 5. (a) High-resolution *Z*-contrast image of the interface between the $Ba_6Ti_{17}O_{40}$ second phase and $BaTiO_3$ grain taken at the $BaTiO_3$ grain tiled to the $[110]_t$ direction. (b) The corresponding image restored by the maximum entropy method. (d) Structure model of the interface, while (c) only shows the positions of the Ba atoms. The interface between $Ba_6Ti_{17}O_{40}$ and $BaTiO_3$ is indicated by zigzag lines in the images and corresponding structure models.

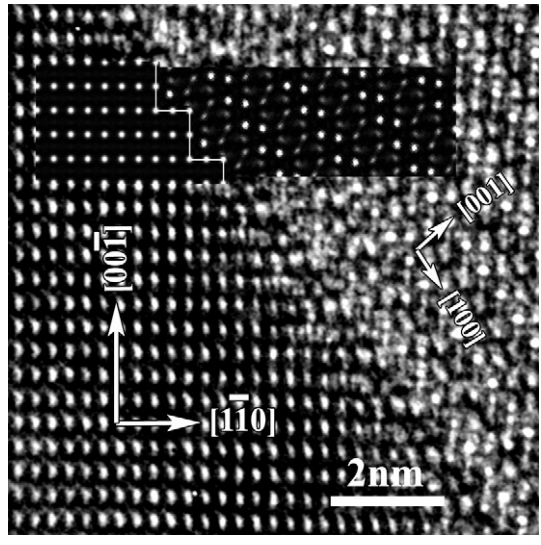

Figure 6. HRTEM image of the same interface shown in figure 5. The inset is a simulation of the HRTEM image, which agrees well with the actual micrograph.

that some bright spots are missing in the vicinity of the boundary, indicated by arrows in figure 5b. This suggests the existence of Ba vacancies (marked by open circles in figure 5c). Nevertheless, the boundary could be considered as a topotactic boundary, where the interface is faceted along the $\{001\}_t$ and $\{110\}_t$ planes of $BaTiO_3$, as well as zigzagged between $(001)_m$ layers 7 and 8 of $Ba_6Ti_{17}O_{40}$. This structure is slightly different from the interface structure proposed by Krasevec *et al*. [22], which is based on the simple crystallographic consideration that the two

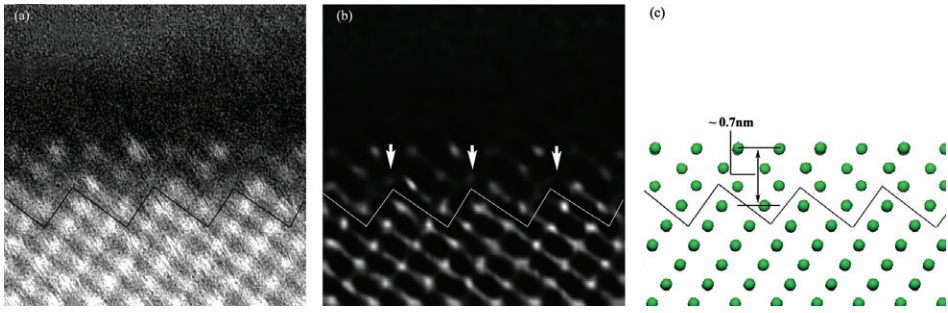

Figure 7. (a) High-resolution *Z*-contrast image of an intergranular layer of a $BaTiO_3$ grain boundary. (b) The corresponding image restored by the maximum entropy method. (c) Structure model of the intergranular layer, which possesses a thickness of ~0.7 nm as marked in the model; only the positions of the Ba atoms are shown.

phases are adjoined with a straight interface at the $\{111\}_t$ plane of $BaTiO_3$ and the $(001)_m$ layer 7 of $Ba_6Ti_{17}O_{40}$.

HRTEM image was also taken on the boundary of $BaTiO_3$ and $Ba_6Ti_{17}O_{40}$ (figure 6). The corresponding simulation was performed using the deduced structure model and it agrees well with the high-resolution micrograph, although the detailed structure at the boundary could not be resolved from the HRTEM image. The reason is that the effects of contrast delocalization and the surface amorphous layer of the TEM specimen, particularly the amorphous layer generated at the free surface of the boundary during TEM sample preparation, are more severe for phase-contrast imaging than *Z*-contrast imaging in the vicinity of the boundary.

At the faceted abnormal GBs in the specimen, intergranular layers could be revealed by *Z*-contrast imaging when the GBs were tilted edge-on (figure 7). This layer has a thickness of ~0.7 nm. Compared with the boundary structure between the $BaTiO_3$ and the $Ba_6Ti_{17}O_{40}$, it can be seen that the intergranular layer has a structure similar to $Ba_6Ti_{17}O_{40}$ and that the layer can be considered as a construction of the $(001)_m$ layers 7, 8, 1, 2 of $Ba_6Ti_{17}O_{40}$. Similar to the boundary between the abnormal $BaTiO_3$ grain and the $Ba_6Ti_{17}O_{40}$ second phase, the interface between the intergranular layer and the abnormal $BaTiO_3$ grain adjoined facets on the $\{001\}_t$ and $\{110\}_t$ planes of the $BaTiO_3$ and the zigzag between the $(001)_m$ layers 7 and 8 of the $Ba_6Ti_{17}O_{40}$ structure. Nevertheless, some bright spots were visible at the interface region, but absent at the boundary between the abnormal $BaTiO_3$ grain and the $Ba_6Ti_{17}O_{40}$ second phase. In the corresponding HRTEM images, the GBs exhibit ordered characteristics although the intergranular layer is hardly distinguishable (figure 8) due to effects, such as contrast delocalization. Although the intergranular layer adjoined the steps on the $\{110\}_t$ and $\{001\}_t$ planes of the $BaTiO_3$ at one side of the layer, the HRTEM image revealed no special interface or orientation relationship between the intergranular layer and the fine $BaTiO_3$ grain at the other side (figure 8). Chemical composition analysis by electron spectroscopic imaging (ESI) revealed Ti-excess at the abnormal GBs. Si concentration was below the detection limit of EDS at the GBs.

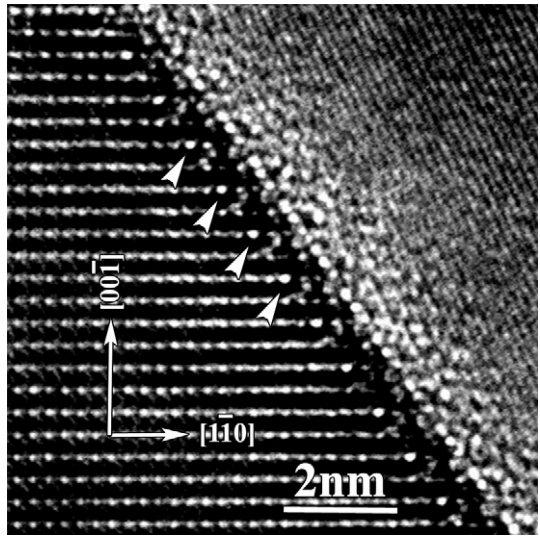

Figure 8. HRTEM image of the intergranular layer shown in figure 7. Periodic bright spots at the interface are indicated by arrows.

As the sample was doped with 0.4 mol% Y, no Y-rich second phase was observed and only slightly Y-segregation (<1%) at the GBs of $BaTiO_3$ was detected by EDS measurement, where the size of the electron probe is ~1 nm.

4. Discussion

Figure 9a shows a side view of the interface structure between $BaTiO_3$ and $Ba_6Ti_{17}O_{40}$, where the viewing direction is $[110]_t$ of $BaTiO_3$. The orientation relationship of $(1\bar{1}\bar{1})_t//(001)_m$, $(1\bar{1}2)_t//(60\bar{2})_m$ and $[110]_t//[0\bar{1}0]_m$ is denoted OR1, hereafter. It can be seen that the TiO_6 octahedra retain the same orientation across the interface and the faceted configuration of $\{100\}_t$ and $\{110\}_t$ is applicable in these circumstances, although rearrangement of the TiO_6 octahedra in the $(001)_m$ plane is needed, as described in [22, 32]. For comparison, a structure model (figure 9b) of the $BaTiO_3/Ba_6Ti_{17}O_{40}$ interface was also constructed following the proposal of Krasevec *et al.* [22] that the orientation relationship is $(\bar{1}1\bar{1})_t//(001)_m$, $(001)_t//(\bar{1}0\bar{1})_m$, $(1\bar{1}0)_t//(20\bar{6})_m$, $[110]_t//[0\bar{1}0]_m$ (henceforth OR2) and the $(\bar{1}1\bar{1})_t$ layer of $BaTiO_3$ adjoins the $(001)_m$ layer 7 of $Ba_6Ti_{17}O_{40}$ at the boundary. It shows that twin elements, i.e. face-shared octahedra, are formed at the interface.

Pirouz *et al.* [33] proposed that preferred orientation relationships between two different crystals correspond to the proximity of the reciprocal lattice points of the two crystals. Their model has been successfully applied to a variety of hetero-interface systems [33–35]. It can be seen from figure 9c and d that there is a high coincidence of reciprocal lattice points of $BaTiO_3$ and $Ba_6Ti_{17}O_{40}$ for OR1 and OR2, although a higher coincidence for OR2 than OR1. This indicates that both OR1 and

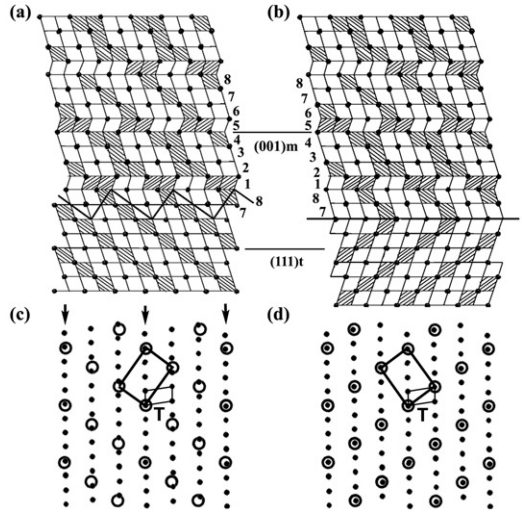

Figure 9. Schematics of the interface structures between $Ba_6Ti_{17}O_{40}$ and $BaTiO_3$, and the corresponding electron diffraction patterns. TiO_6 octahedra are hatched *per* [22] in (a) and (b). Open and solid circles indicate the reciprocal lattice points of crystalline $BaTiO_3$ and $Ba_6Ti_{17}O_{40}$, respectively, in (c) and (d). Here, (a) and (c) correspond to the structure model for OR1; (b) and (d) represent OR2. The viewing direction is $[110]_t$ of $BaTiO_3$. In (c), the rows in which the reciprocal lattice points of $Ba_6Ti_{17}O_{40}$ and $BaTiO_3$ are highly coincident are indicated by arrows.

OR2 are possibly favourable orientation relationships, while OR2 may be more favourable. This was proved in polycrystalline $Ba_6Ti_{17}O_{40}$, formed by chemical deposition of SiO_2 on a single crystal $BaTiO_3$ substrate, where both OR1 and OR2 were observed [23], as well as in other studies on $Ba_6Ti_{17}O_{40}$ second phase in $BaTiO_3$ ceramics, where OR2 was mainly found [18, 20–22]. For the epitaxial growth of a thin film on a substrate, the energy of the film/substrate interface plays an important role in total interfacial energy [36]. OR2 forms face-shared octahedra at the interface, which represent an unstable arrangement [32]. In contrast, OR1 has the TiO_6 octahedra aligned in the same orientation across the interface; therefore, OR1 is more favourable for $Ba_6Ti_{17}O_{40}$ thin film epitaxially grown on $BaTiO_3$ substrate.

When sintering was performed above the eutectic temperature of $BaTiO_3$ and $Ba_6Ti_{17}O_{40}$ or slightly below the eutectic point but with (intended) additives of CaO, Al_2O_3 or SiO_2, a liquid phase was believed to form and $Ba_6Ti_{17}O_{40}$ was often observed at triple junctions of the $BaTiO_3$ grains with an angle less than 60° between round grains of $BaTiO_3$ [15, 18, 19]. However, $Ba_6Ti_{17}O_{40}$ was also observed at sintering well below the eutectic temperature of $BaTiO_3$ and $Ba_6Ti_{17}O_{40}$, and it is believed that the second phase was formed with no liquid phase involved, although it is possible that the eutectic point may decrease with the presence of impurities, such as SiO_2 and Al_2O_3 [20, 21]. In our experiment, the sintering temperature (1300°C) is below the eutectic point and the Si concentration is below the detection limit of the EDS analysis in the second phase. In our study, a characteristic of $Ba_6Ti_{17}O_{40}$ second phase was that it had a planar boundary with the $\{111\}_t$ plane of the abnormal grain

(at μm- but not atomic-scale) and appeared plate-shaped on the substrate of the abnormal grain; the two matrix grains were not faceted on low indexed planes at the triple-grain junction. Therefore, it is possible that the second phase is not formed by solidification of the liquid phase but by surface diffusion of ions on the surface of the particles during sintering, as surface diffusion became the prevailing mechanism of mass transfer at a temperature just below which the liquid phase appears, as suggested in [32]. Hence, it is reasonable to expect that $Ba_6Ti_{17}O_{40}$ layers will grow epitaxially on the surface of $BaTiO_3$ and form the plate-shaped second phases. The intergranular layers could be formed in a similar way. Nevertheless, we cannot rule out the possible presence of a liquid phase during sintering, as the sintering temperature is close to the eutectic point plus the possible existence of impurities in the material. As mentioned in section 1, *Lee et al*. [8] observed an intermediate layer at the GBs of TiO_2-excess $BaTiO_3$ and suggested that the presence of the intermediate phase assisted the abnormal growth of the $BaTiO_3$ grains.

Y^{3+} preferentially locates at the Ba^{2+} lattice sites forming a donor cation in TiO_2-excess $BaTiO_3$ or at the Ti^{4+} lattice sites forming an acceptor cation in BaO-excess $BaTiO_3$ [37]. Xue *et al*. [38] showed that Y^{3+} occupied the Ba^{2+} sites when low levels of Y_2O_3 were doped into stoichiometric $BaTiO_3$. Meanwhile, Chiang *et al*. [7, 39] used STEM to measure the chemical composition of GBs in doped barium and strontium titanates, and concluded that donor dopants were only found for slight segregation at GBs, although acceptor dopants segregated significantly. The interpretation was that the GB space-charge distribution consisted of a positive boundary charge and negative space-charge [7]. The acceptor dopants (negative effective charge) segregate in the negative space-charge region driven by the electrostatic potential, while the donor dopants (positive effective charge) are depleted. Compared with acceptor donor segregation, depletion of the donors is hard to detect owing to the small absolute magnitude of the decrease in concentration and possible compensation by the slight donor segregation to the positive charge GB core; the two regions are hardly distinguishable by microanalysis [7]. Ti-excess was observed at all GBs of the doped titanates examined and was presumably (partially) responsible for the positive boundary and negative space-charge [7]. The results of this work show that there is no significant segregation of Y^{3+} at the grain boundary region. This suggests that Y^{3+} is predominantly present the Ba^{2+} lattice sites, while the concentration of Y^{3+} at Ba^{2+} sites is $\leq$0.4 at%, which is below the solubility of Y^{3+} at the Ba^{2+} sites in $BaTiO_3$ of $\sim$1.5 at% [37, 40]. Our observation of Ti-excess at the GBs is consistent with the model of a positive boundary and negative space-charge. Another possible reason for Y^{3+} incorporate into the Ba^{2+} sublattice in the samples is BaO loss by evaporation during sintering [41]. As a result, the samples may become TiO_2-excess, although the initial composition of (Ba + Y) is slightly higher than that of Ti.

Abnormal grain growth was often observed in doped $BaTiO_3$ at low dopant concentrations, while grain growth was suppressed at higher dopant additions [42, 43]. Grain growth inhibition was attributed either to the transition of charge compensation from electrons to cation vacancies [44] or to the incorporation of dopants into the $BaTiO_3$ lattice [43]. The abnormal grain growth observed in the Y-doped $BaTiO_3$ samples agrees with previous results.

5. Conclusions

TEM and STEM investigations show small plate-shaped, second phase $Ba_6Ti_{17}O_{40}$ located at triple-grain junctions in Y-doped polycrystalline $BaTiO_3$ ceramics. Using electron diffraction techniques, an orientation relationship was determined between the tetragonal $BaTiO_3$ and the monoclinic $Ba_6Ti_{17}O_{40}$ as $(1\bar{1}\bar{1})_t//(001)_m$, $(1\bar{1}2)_t//(60\bar{2})_m$, and $[110]_t//[0\bar{1}0]_m$. High-resolution *Z*-contrast imaging revealed atomic steps on the $\{110\}_t$ and $\{001\}_t$ planes of $BaTiO_3$ at the boundary between the $BaTiO_3$ grain and the $Ba_6Ti_{17}O_{40}$ second phase.

An intermediate layer was observed at grain boundaries in the Y-doped $BaTiO_3$, which was determined by *Z*-contrast and electron spectroscopic imaging as a Ti-rich phase with a crystal structure similar to $Ba_6Ti_{17}O_{40}$.

Acknowledgments

SJZ and XLM are grateful to the National Outstanding Young Scientist Foundation for Grant No. 50325101 (XLM) and Special Funds for the Major State Basic Research Projects of China (Grant No. 2002CB613503) for the financial support. KD and XHS thank the Natural Sciences Foundation of China for support under Grant No. 50601027.

References

[1] B. Huybrechts, K. Ishizaki and M. Takata, J. Mater. Sci. **30,** 2463 (1995).
[2] H. Kishi, Y. Mizuno and H. Chazono, Jpn. J. Appl. Phys. **42,** 1 (2003).
[3] A. Feteira, D.C. Sinclair, I.M. Reaney, *et al*., J. Am. Ceram. Soc. **87,** 1082 (2004).
[4] R.D. Roseman and N. Mukherjee, J. Electroceram. **10,** 117 (2003).
[5] H. Nemoto and I. Oda, J. Am. Ceram. Soc. **63,** 398 (1980).
[6] D.Y. Wang and K. Umeya, J. Am. Ceram. Soc. **73,** 669 (1990).
[7] Y.-M. Chiang and T. Takagi, J. Am. Ceram. Soc. **73,** 3278 (1990).
[8] S.B. Lee, W. Sigle and M. Ruhle, Acta Mater. **50,** 2151 (2002).
[9] T. Yamamoto, Y. Ikuhara, K. Hayashi, *et al*., J. Mater. Res. **13,** 3449 (1998).
[10] T. Yamamoto, K. Hayashi, Y. Ikuhara, *et al*., Phil. Mag. Lett. **79,** 327 (1999).
[11] K. Hayashi, T. Yamamoto, Y. Ikuhara, *et al*., J. Am. Ceram. Soc. **83,** 2684 (2000).
[12] Y.K. Cho, S.J.L. Kang and D.Y. Yoon, J. Am. Ceram. Soc. **87,** 119 (2004).
[13] S.Y. Choi, D.Y. Yoon and S.J.L. Kang, Acta Mater. **52,** 3721 (2004).
[14] S.Y. Choi, S.J.L. Kang, S.Y. Chung, *et al*., Appl. Phys. Lett. **88,** 011909 (2006).
[15] L. Affleck and C. Leach, J. Eur. Ceram. Soc. **25,** 3017 (2005).
[16] J. Seaton and C. Leach, Acta Mater. **53,** 2751 (2005).
[17] S.B. Desu and D.A. Payne, J. Am. Ceram. Soc. **73,** 3398 (1990).
[18] M.H. Lin and H.Y. Lu, Acta Mater. **50,** 605 (2002).
[19] A. Belous, O. V'Yunov, L. Kovalenko, *et al*., J. Solid State Chem. **178,** 1367 (2005).
[20] D. Makovec and D. Kolar, J. Am. Ceram. Soc. **80,** 45 (1997).
[21] D. Makovec and M. Drofenik, J. Am. Ceram. Soc. **83,** 2593 (2000).
[22] V. Krasevec, M. Drofenik and D. Kolar, J. Am. Ceram. Soc. **70,** C193 (1987).

[23] S. Senz, A. Graff, W. Blum, *et al*., J. Am. Ceram. Soc. **81,** 1317 (1998).
[24] M.M. McGibbon, N.D. Browning, A.J. McGibbon, *et al*., Phil. Mag. A **73,** 625 (1996).
[25] M.F. Chisholm and S.J. Pennycook, Phil. Mag. **86,** 4699 (2006).
[26] S. Hillyard and J. Silcox, Ultramicroscopy **58,** 6 (1995).
[27] P.D. Nellist and S.J. Pennycook, Ultramicroscopy **78,** 111 (1999).
[28] S.F. Gull and J. Skilling, IEE Proc. F, Commun. Radar Signal Process. **131,** 646 (1984).
[29] A.J. McGibbon, S.J. Pennycook and D.E. Jesson, J. Microsc. **195,** 44 (1999).
[30] T. Negas, R.S. Roth, H.S. Parker, *et al*., J. Solid State Chemistry **9,** 297 (1974).
[31] P.D. Nellist and S.J. Pennycook, Adv. Imag. Electron Phys. **113,** 147 (2000).
[32] V. Krasevec, M. Drofenik and D. Kolar, J. Am. Ceram. Soc. **73,** 856 (1990).
[33] P. Pirouz, Y. Ikuhara and F. Ernst, in *Interface Science and Materials Interconnection, JIMIS-8*, edited by Y. Ishida (The Japan Institute of Metals, Tokyo, 1996), p. 107.
[34] S. Stemmer, P. Pirouz, Y. Ikuhara, *et al*., Phys. Rev. Lett. **77,** 1797 (1996).
[35] F. Ernst and J.A. Switzer, Z. Metallk. **94,** 259 (2003).
[36] A.P. Sutton and R.W. Balluffi, Acta Metall. **35,** 2177 (1987).
[37] D. Makovec, Z. Samardzija and M. Drofenik, J. Am. Ceram. Soc. **87,** 1324 (2004).
[38] L.A. Xue, Y. Chen and R.J. Brook, Mater. Sci. Eng. B **1,** 193 (1988).
[39] Y.-M. Chiang and T. Takagi, J. Am. Ceram. Soc. **73,** 3286 (1990).
[40] J. Zhi, A. Chen, Y. Zhi, *et al*., J. Am. Ceram. Soc. **82,** 1345 (1999).
[41] J.S. Chun, N.M. Hwang, D.Y. Kim, *et al*., J. Am. Ceram. Soc. **87,** 1779 (2004).
[42] L.A. Xue, Y. Chen and R.J. Brook, J. Mater. Sci. Lett. **7,** 1163 (1988).
[43] J.K. Lee, K.S. Hong and J.H. Chung, J. Am. Ceram. Soc. **84,** 1745 (2001).
[44] C.-J. Peng and H.-Y. Lu, J. Am. Ceram. Soc. **71,** C44 (1988).